

# Spectral methods in general relativity – toward the simulation of 3D–gravitational collapse of neutron stars

S. Bonazzola

J. Friebe<sup>\*</sup>

E.ourgoulhon

J.A. Marck

## Abstract

Several applications of spectral methods to problems related to the relativistic astrophysics of compact objects are presented. Based on a proper definition of the analytical properties of regular tensorial functions we have developed a spectral method in a general spherical-like coordinate system. The applications include the investigation of spherically symmetric neutron star collapse as well as the solution of the coupled 2D–Einstein–Maxwell equations for magnetized, rapidly rotating neutron stars. In both cases the resulting codes are efficient and give results typically several orders of magnitude more accurate than equivalent codes based on finite difference schemes. We further report the current status of a 3D–code aiming at the simulation of non-axisymmetric neutron star collapse where we have chosen a tensor based numerical scheme.

**Key words:** spectral methods, numerical relativity, neutron stars, black holes, gravitational collapse.

**AMS subject classifications:** 65M70, 65N35, 83–08.

## 1 Introduction

Compact objects in astrophysics such as neutron stars and black holes are subjected to the strong field regime of gravitation and have hence to be treated within the framework of general relativity. The growing interest in the numerical solution of the Einstein equations for astrophysically relevant systems has given rise to a new branch of computational physics – *numerical relativity* [1, 2, 3]. This development is due to the increasingly powerful computational resources which make these problems accessible to a numeri-

<sup>\*</sup>Département d’Astrophysique Relativiste et de Cosmologie (UPR 176 du CNRS), Observatoire de Paris, Section de Meudon, F–92195 Meudon Cedex, France, e-mail: frieben@obspm.fr

ICOSAHOM’95: Proceedings of the Third International Conference on Spectral and High Order Methods. ©1996 Houston Journal of Mathematics, University of Houston.

cal investigation. It is further stimulated by the prospects of gravitational wave astronomy which will turn into an observational science toward the end of this decade thanks to gravitational wave observatories like LIGO, VIRGO and GEO600 that are now under construction [4, 5, 6].

We use the (3+1)–formalism of general relativity [7] which consists in foliating spacetime into a sequence of space-like hypersurfaces which represent curved 3–space at a fixed coordinate time  $t$ . The fabric of spacetime is then determined by the 3–metric  $h_{ij}$  and four additional quantities, the *lapse function*  $N$  and the *shift vector*  $N^i$  which fix the propagation of the space-like hypersurfaces in time and the change of the spatial coordinate system between adjacent hypersurfaces. This Hamilton type approach to general relativity results in a temporal first order evolution scheme for the dynamical variables which is completed by some constraint equations which ensure the consistency of gravitational and matter fields. Furthermore  $N$  and  $N^i$  have to be determined by the choice of appropriate gauge conditions which typically lead to elliptic equations that have to be solved at each time step. For stationary configurations all time derivatives vanish and one obtains a system of coupled elliptic equations for the gravitational fields. The efficient solution of elliptic equations is hence of central interest for us.

Let us consider a covariant Poisson equation  $N^{i|_i} = S$  in a conformally flat axisymmetric space where the line element reads

$$(1) \quad dl^2 = A^4(r, \theta) (dr^2 + r^2 d\theta^2 + r^2 \sin^2\theta d\phi^2).$$

The former equation can be rewritten to yield a Poisson-like equation for  $N$  where we have isolated the flat space Laplacian  $\Delta_f$  and contributed the curvature terms to the source. Here  $\alpha$  denotes  $\ln A$ .

$$(2) \quad \Delta_f N = \tilde{S} \quad \text{with} \quad \tilde{S} = A^4 S - 2(\partial_r \alpha \partial_r N + \frac{1}{r^2} \partial_\theta \alpha \partial_\theta N).$$

This equation has to be solved by iteration. The solution of  $\Delta_f N = \tilde{S}$  at each iteration has hence to be accomplished sufficiently fast in order to keep the total computation cost at a reasonable level.

After outlining the basic features of our spectral method [8, 9], we will proceed in a first step to the investigation of black hole formation due to spherically symmetric neutron star collapse which has proved the high aptitude of spectral methods in this field [10, 11, 12]. The second part is devoted to the study of axisymmetric stationary rotating bodies which has been applied to model rapidly rotating neutron stars [13, 14]. This work has been extended recently to include strong magnetic fields for the first time into neutron star models [15]. Special emphasis in all cases has been put on the extensive use of external and intrinsic tests [16, 17, 18] of the self-consistency and the attained accuracy of the numerical results. The resulting neutron star models provide us with the required initial value models for the investigation of 3D-gravitational collapse of neutron stars which will reveal the whole range of gravitational wave emission associated with this phenomenon. We give an overview about the inset of spectral methods in this project which is currently in work. Here a new method for the efficient inversion of a generalized 3D-vector Poisson equation is a first major result.

## 2 Spectral methods in general relativity

### 2.1 Coordinates and regularity conditions

The space-like hypersurfaces stemming from the former choice of the (3+1)-formalism are conceived to describe some asymptotically flat space, containing a compact, mostly starlike object. The natural choice is thus a spherically coordinate system  $(r, \theta, \phi)$ .

The pseudo-singularities which appear in this case can be overcome by a proper definition of regularity conditions of tensorial quantities. A consequent application of parity rules derived from these conditions allows further to optimize code efficiency and precision.

We consider the related Cartesian type coordinate system  $(x, y, z) = (r \sin \theta \cos \phi, r \sin \theta \sin \phi, r \cos \theta)$ . We define a tensorial quantity  $T_{i_1 \dots i_N}$  in spherical coordinates  $(r, \theta, \phi)$  to be *regular*, if its components  $f_{i_1 \dots i_N}$  with respect to Cartesian coordinates  $(x, y, z)$  are regular in the sense that they can be expanded into a polynomial sum of the type

$$(3) \quad f_{i_1 \dots i_N}(x, y, z) = \sum_{i, j, k=0}^N a_{i_1 \dots i_N i j k} x^i y^j z^k$$

which can be written in terms of  $(r, \theta, \phi)$  as

$$(4) \quad \tilde{f}_{i_1 \dots i_N}(r, \theta, \phi) = \sum_{i, j, k=0}^N a_{i_1 \dots i_N i j k} r^{i+j+k}$$

$$\times \sin^{i+j} \theta \cos^k \theta \cos^i \phi \sin^j \phi.$$

Having specified the tensor components  $f_{i_1 \dots i_N}$  with respect to the Cartesian frame we derive the components related to the local orthonormal frame of spherical coordinates by a *non-singular* coordinate transformation.

In order to infer the analytical properties of a scalar function it is useful to rearrange the sum in (4). We first collect all the terms referring to  $\cos m\phi$  and  $\sin m\phi$  respectively. We write

$$(5) \quad \tilde{f}(r, \theta, \phi) = \sum_{m=0}^M (a_m(r, \theta) \cos m\phi + b_m(r, \theta) \sin m\phi)$$

where  $a_m(r, \theta)$  and  $b_m(r, \theta)$  behave identically in the further procedure. We opt for  $\cos l\theta$  and  $\sin l\theta$  as basis functions in  $\theta$  which allows the application of FFT-techniques for this transformation. An immediate conclusion from (4) and the case  $i+j$  even is that the coefficients  $a_{2m}(r, \theta)$  and  $b_{2m}(r, \theta)$  have to be expanded in terms of  $\cos l\theta$  while from the odd case that the expansion of  $a_{2m+1}(r, \theta)$  and  $b_{2m+1}(r, \theta)$  has to be done on the set  $\sin l\theta$ . We therefore specify

$$(6) \quad a_{2m}(r, \theta) = \sum_{l=0}^L \tilde{a}_{l, 2m}(r) \cos l\theta,$$

$$(7) \quad a_{2m+1}(r, \theta) = \sum_{l=0}^L \tilde{a}_{l, 2m+1}(r) \sin l\theta.$$

Note that due to the well defined parity of  $a_{2m}$  and  $a_{2m+1}$  these coefficients – a priori only defined for  $0 \leq \theta \leq \pi$  – can be continued analytically to periodic functions of  $\theta$  on the interval  $[-\pi, \pi]$ .

In the same manner as before we find from (4) that the polynomials  $\tilde{a}_l(r)$  are symmetric with respect to the inversion  $r \rightarrow -r$  for  $l$  even and antisymmetric for  $l$  odd. As basis function set in  $r$  we decide for Chebyshev polynomials due to their superior properties in finite approximation schemes of non-periodic functions and the availability of fast Chebyshev transforms. Simplifications of the expansion scheme in the presence of additional symmetries are precised in the following paragraphs.

Any regular function admits an expansion of this kind, but regularity furthermore implies additional constraints on the different coefficients. Having set up regular initial data according to (3), regularity of the involved quantities is maintained during a calculation by the application of regular operators – we here ignore the influence of numerical effects due to aliasing or roundoff errors.

Let us consider the covariant derivative of a vector in spherical coordinates. For the scalar potential  $U(r, \theta, \phi) =$

$r \sin \theta \cos \phi$  and

$$(8) \quad U_{|i} = (\partial_r U, \frac{1}{r} \partial_\theta U, \frac{1}{r \sin \theta} \partial_\phi U)$$

we have

$$(9) \quad (U_r, U_\theta, U_\phi) = (\sin \theta \cos \phi, \cos \theta \cos \phi, -\sin \phi).$$

The covariant derivative  $U_{\theta|\phi}$  which reads

$$(10) \quad U_{\theta|\phi} = \frac{1}{r \sin \theta} \partial_\phi U_\theta - \frac{1}{r \tan \theta} U_\phi$$

can be rewritten to yield

$$(11) \quad U_{\theta|\phi} = \frac{1}{r \sin \theta} (\partial_\phi U_\theta - \cos \theta U_\phi).$$

A numerical evaluation according to (8) and (11) reveals a perfectly regular behavior.

## 2.2 Supersymmetric case

Additional spatial symmetries of physical systems involve continuous symmetry operations like rotation about a distinct axis with an associated Killing vector field or discrete transformations like inversion at the equatorial plane  $z=0$ , leading to distinct parity properties of the different tensor components.

We define *supersymmetry* [19] by the following behavior of a scalar function:  $f$  is invariant with respect to inversion at the  $z$ -axis, hence  $f(-x, -y, z) = f(x, y, z)$ , while  $f$  is [anti-] symmetric with respect to reflection at the equatorial plane  $z=0$ , hence  $f(x, y, -z) = \pm f(x, y, z)$ . Consequently  $f$  can be expanded into a sum of the type

$$(12) \quad f_+(x, y, z) = \sum_{l=0}^L \sum_{k=0}^{2l} \sum_{m=0}^M c_{klm} x^{2l-k} y^k z^{2m} \text{ even case}$$

$$(13) \quad f_-(x, y, z) = \sum_{l=0}^L \sum_{k=0}^{2l} \sum_{m=0}^M c_{klm} x^{2l-k} y^k z^{2m+1} \text{ odd case}$$

which defines subsets of the general scalar functions introduced in Sec. 2.1. A write-up in terms of  $(r, \theta, \phi)$  gives

$$(14) \quad \tilde{f}_+(r, \theta, \phi) = \sum_{l=0}^L \sum_{k=0}^{2l} \sum_{m=0}^M c_{klm} r^{2(l+m)} \times \sin^{2l} \theta \cos^{2m} \theta \cos^{2l-k} \phi \sin^k \phi,$$

$$(15) \quad \tilde{f}_-(r, \theta, \phi) = \sum_{l=0}^L \sum_{k=0}^{2l} \sum_{m=0}^M c_{klm} r^{2(l+m)+1} \times \sin^{2l} \theta \cos^{2m+1} \theta \cos^{2l-k} \phi \sin^k \phi$$

which can be modified, replacing  $\sin^2 \theta$  by  $(1 - \cos^2 \theta)$ .

$$(16) \quad \tilde{f}_+(r, \theta, \phi) = \sum_{l=0}^L \sum_{k=0}^{2l} \sum_{m=0}^M c_{klm} r^{2(l+m)} \times (1 - \cos^2 \theta)^l \cos^{2m} \theta \cos^{2l-k} \phi \sin^k \phi,$$

$$(17) \quad \tilde{f}_-(r, \theta, \phi) = \sum_{l=0}^L \sum_{k=0}^{2l} \sum_{m=0}^M c_{klm} r^{2(l+m)+1} \times (1 - \cos^2 \theta)^l \cos^{2m+1} \theta \cos^{2l-k} \phi \sin^k \phi.$$

According to Sec. 2.1 we conclude for the decomposition of a supersymmetric function:

1.  $f$  is  $\pi$ -periodic in the angular variable  $\phi$ ,
2.  $a_{2m}(r, \theta)$  has to be expanded into a sum of  $\cos l\theta$  where  $l$  is even in the symmetric case and odd in the anti-symmetric one,
3.  $\tilde{a}_l(r)$  is an even polynomial in  $r$  for  $f$  symmetric and an odd polynomial for  $f$  antisymmetric.

Physical problems which imply the use of supersymmetric functions allow to restrict the computational domain to  $[0, \pi]$  in  $\phi$  and to  $[0, \pi/2]$  in  $\theta$  which leads to an overall reduction of the effective grid size by a factor four.

For the components of a vector field associated with the case of even supersymmetry we conclude:  $U_r$  can be expanded into a sum of  $\cos 2l\theta$ ,  $U_\theta$  into a sum of  $\sin 2l\theta$  and  $U_\phi$  into a sum of  $\sin(2l+1)\theta$  which means that  $U_\theta$  undergoes a change of sign by reflection at the equatorial plane while  $U_r$  and  $U_\phi$  remain unchanged. The expansion of the radial part is done in terms of odd powers of  $r$  for all components.

## 2.3 Axisymmetric case

Axisymmetry restricts the set of scalar functions under consideration to functions according to Sec. 2.1 where the only remaining term in (5) is  $a_0(r, \theta)$ . Thus  $f$  can be written as

$$(18) \quad f(r, \theta) = \sum_{l=0}^L \tilde{a}_{l,0}(r) \cos l\theta$$

where  $\tilde{a}_{l,0}(r)$  is an even function in  $r$  for  $l$  even and an odd function for  $l$  odd.

For the components  $U_r$  and  $U_\theta$  of a vector field compatible with the assumption of axisymmetry we conclude:  $U_r$  has to be expanded in terms of  $\cos l\theta$  where the radial part is even for  $l$  odd and odd for  $l$  even.  $U_\theta$  has to be expanded in terms of  $\sin l\theta$  where we also have a parity change in  $r$ .

The properties of the lacking component  $U_\phi$  which we need to handle  $N_\phi$  in the models of rotating neutron stars can be derived from the Killing equation linked to axisymmetry. A short examination reveals that  $U_\phi$  has to be expanded in terms of  $\sin l\theta$  with a parity change in  $r$  – it behaves identically as  $U_\theta$ .

## 2.4 Spherically symmetric case

For sake of completeness we add the spherically symmetric case. As a further restriction of the axisymmetric case we keep from (18) only  $\tilde{a}_{0,0}(r)$ .  $f(r)$  therefore reads

$$(19) \quad f(r) = \sum_{k=0}^K a_{2k} r^{2k}$$

which is an ordinary even polynomial in  $r$  while  $U_r$  is represented by an odd polynomial in  $r$ .

## 3 Spherically symmetric neutron star collapse

### 3.1 Basic equations

The investigation of neutron star equilibrium configurations in spherical symmetry was the first problem in the fully general relativistic regime being solved by us by means of the (3+1)–formalism of general relativity and a spectral method [10, 8, 9]. A favorable choice of the line element  $ds^2 = g_{\alpha\beta} dx^\alpha dx^\beta$  in the case of spherical symmetry is given by RGPS (*Radial Gauge–Polar Slicing*) coordinates [20] and reads

$$(20) \quad ds^2 = -N^2 dt^2 + A^2 dr^2 + r^2 (d\theta^2 + \sin^2\theta d\phi^2).$$

We stress the particular nature of this problem where the field variable  $A$  is not really a dynamical quantity. In fact it is uniquely determined at any moment as well as the lapse function  $N$  by the matter fields which have to be evolved by means of the hydrodynamical equations. Since the solution outside the star is known in advance to coincide with the *static* Schwarzschild solution of a point mass of the same size according to the *Birkhoff theorem*, we benefit from a double simplification. First the whole time evolution is yet determined by propagating the hydrodynamical variables and further the calculation can be restricted to the stellar interior. The interior solution for the gravitational field has then to be matched to the analytical exterior one. We further note that due to the static character of the exterior solution no gravitational waves – which otherwise would be an observable of most importance – are emitted.

Concerning the hydrodynamical part we employ a set of particular variables which lead to equations resembling very closely their Newtonian counterparts including a general relativistic generalization of the classical Euler equation. We note the privileged role of the Eulerian or local rest observer  $\mathcal{O}_0$  in this formulation. The hydrodynamical equations read

$$(21) \quad \partial_t \mathcal{E} + \frac{1}{r^2} \partial_r (r^2 (\mathcal{E} + p) V^r) = 0,$$

$$(22) \quad \partial_t U + V^r \partial_r U = -\frac{1}{\mathcal{E} + p} \left( \frac{N}{A} \partial_r p + U \partial_t p \right) - \frac{AN}{\Gamma^2} \left( \frac{m}{r^2} + 4\pi r p \right),$$

$$(23) \quad \partial_t D + \frac{1}{r^2} \partial_r (r^2 D V^r) = 0,$$

$$(24) \quad \partial_t s_B + V^r \partial_r s_B = 0$$

where we have introduced the energy density  $\mathcal{E}$  and the fluid velocity  $U$  measured by  $\mathcal{O}_0$ , the coordinate baryon density  $D$  and the entropy per baryon  $s_B$  while  $V^r$  denotes the fluid coordinate velocity. The Lorentz factor  $\Gamma$  is defined as  $\Gamma = (1 - U^2)^{-\frac{1}{2}}$ . In addition one has to solve

$$(25) \quad \partial_r m(r, t) = 4\pi r^2 \mathcal{E}(r, t),$$

$$(26) \quad \partial_r \Phi(r, t) = A^2 \left( \frac{m(r, t)}{r^2} + 4\pi r [p + (\mathcal{E} + p) U^2] \right)$$

where  $A(r, t)$  is related to  $m(r, t)$  through

$$(27) \quad A(r, t) = \left( 1 - \frac{2m(r, t)}{r} \right)^{-\frac{1}{2}}.$$

The neutron star matter is modeled as a perfect fluid, adopting a realistic dense matter equation of state.

### 3.2 Numerical method

The initial value model for the dynamical calculations is provided by solving the Tolman–Oppenheimer–Volkoff equations describing a spherically symmetric static star where each model is determined by the central value of the pseudo-enthalpy  $H_c$ . A first solution is obtained by integration of this system of ordinary differential equations while an overall numerical accuracy of the order of  $10^{-14}$ , adapted to the subsequent use of a spectral method, is achieved by iteration of the approximate solution.

The computational domain is identical with the stellar interior during the whole calculation, thanks to a comoving grid whose outer boundary coincides with the star surface.

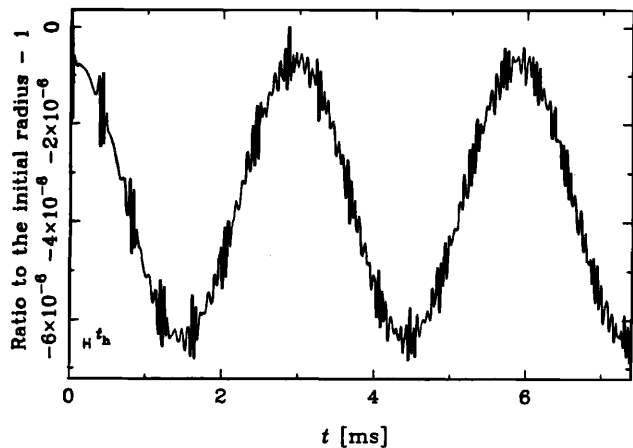


Figure 1: Relative variation of the stellar radius with elapsing time for a stable equilibrium model with  $n_B < n_B^{\text{crit}}$  and  $|\Delta M/M_{\text{max}}| = -5 \times 10^{-5}$ . The hydrodynamical timescale is indicated on the lower left.

This maintains a constant spatial resolution during the collapse and a fine sampling of the steepening gradients near the star surface thanks to the accumulation of the Gauß-Lobatto points in this region. It furthermore minimizes the advective terms, hence improving the numerical accuracy. All quantities are expanded in terms of Chebyshev polynomials in  $r$  mapping the interval  $[0, R_*(t)]$  onto  $[0, 1]$  taking into account their analytical properties according to Sec. 2.4. The 2<sup>nd</sup> order semi-implicit time integration ensures the stability of the code which allows us to perform simulations of a duration of many dynamical timescales. This ability is very important when studying the effects of perturbations on equilibrium configurations. This task is also favored by the fact that we integrate the original system of equations without any artificial viscosity to stabilize the code while in addition the intrinsic viscosity of the hydrodynamical system at  $r = R_*$  gives rise to one boundary condition which is chosen to fix the baryon density at the star boundary. It is imposed by means of a  $\tau$ -Lanczos procedure [21] on the system as a whole which is the well posed mathematical procedure.

### 3.3 Results

Among the various tests we have imposed on our code one describes the collapse of a homogeneous dust sphere whose solution was given by Oppenheimer and Snyder [22]. From

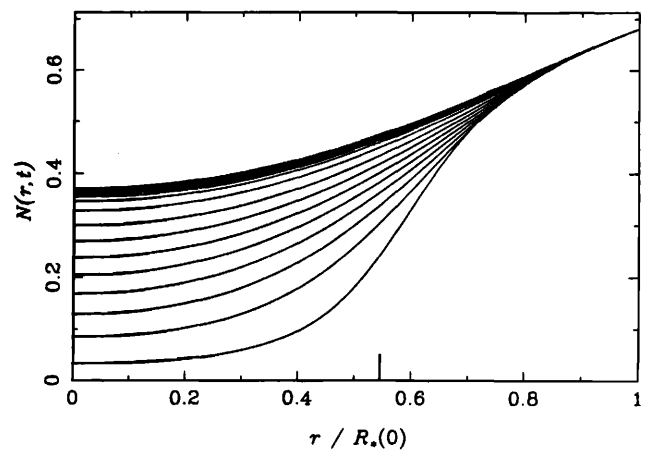


Figure 2: Profiles of the lapse function  $N$  for  $t$  ranging from 0 to 7.296 ms. The location of the Schwarzschild radius  $R_S$  is indicated by a vertical bar. Direction of increasing time is downward.

the beginning of the collapse until the moment where the whole configuration is highly relativistic and practically frozen we observed the different variables to reproduce the analytical values within an error of better than  $10^{-5}$  [10], while the errors related to previous studies based on finite difference methods are of the order of  $10^{-2}$  [23].

Neutron star models near the maximum mass configuration –  $M_{\text{max}} = 1.924M_{\odot}$  and  $R = 10.678$  km for the employed EOS – are interesting with respect to their stability against radial perturbations. Configurations with a central baryon density approaching the critical one exhibit an oscillatory behavior which is dominated by the *fundamental* mode of oscillation of increasing period length. It represents a uniform growing and shrinking of the entire star which is modulated by less important harmonics of higher order. Fig. 1 shows this temporal variation for a stable configuration. We stress that these oscillations are entirely driven by roundoff and discretization errors of a total order of  $10^{-10}$  – no external force has been applied to trigger this variability. Increasing the central baryon density beyond the critical value one enters the branch of unstable configurations. This time the fundamental mode starts a contraction of the star which results in an unlimited collapse. Though the actual coordinate choice is not capable to properly capture the formation of an apparent horizon which would clearly reveal the formation of a black hole the evolution of metric potentials and matter variables gives a distinct indication of this event. Take for

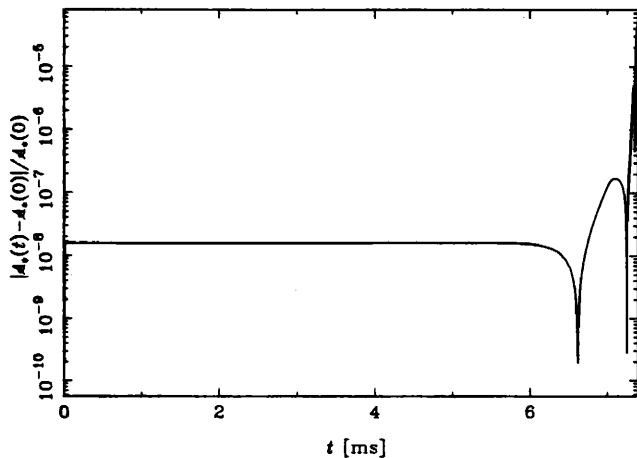


Figure 3: Relative variation of the total baryon number during the collapse.

instance Fig. 2 which shows the time development of the lapse function  $N$ , measuring the elapsed proper time of the local Eulerian observer  $\mathcal{O}_0$ . Inside the Schwarzschild radius it tends toward zero for increasing coordinate time  $t$ . This behavior – called the ‘*lapse of the lapse*’ – is related to the singularity avoidance property of the chosen coordinate gauge which keeps the spatial hypersurfaces from propagating into a forming singularity. The dynamical timescale of the collapse is the time elapsed from the beginning of the collapse until the moment where the evolution appears to be frozen to a distant observer and has the value  $t = 7.4$  ms for the considered configuration. Fig. 3 illustrates the relative error committed on the total baryon number which is a conserved global quantity. In the early phase it is conserved with a relative accuracy of  $2 \times 10^{-8}$  and with  $4 \times 10^{-6}$  during the violent stages of the collapse. The deviation increases up to  $5 \times 10^{-5}$  in the final phase where sharp gradients form near the horizon. The proper working of the code in the perturbative regime has been recently confirmed by direct comparison with a linear adiabatic code [12]. The calculations have shown a very good agreement of the frequencies of the fundamental modes for the two opposite approaches. The original version of our code has been extended later on to include the processes of neutrino production and transport during neutron star collapse in order to compute the observable neutrino emission for a distant observer [11]. A multi-domain extension of this code is in use in order to simulate type II supernovae in spherical symmetry. It is particularly well suited to properly capture the high contrast up to  $\simeq 10^6$  of the mean

densities in the individual subdomains which appears during the collapse. Four to five zones are typically needed to cover the dense central core forming the new born neutron star and the outer layers of much lower density with the desired resolution. In contrast with the original code boundary conditions are imposed in this case by means of a modified  $\tau$ -Lanczos scheme applied in *coefficient* space.

## 4 Axisymmetric rotating relativistic bodies

### 4.1 Basic equations

In order to study rapidly rotating neutron stars we have made the assumptions of spacetime being *axisymmetric*, *stationary* and *asymptotically flat*. We have further supposed spacetime to be *circular*, thus the absence of meridional currents in the sources of the gravitational field. In this case spacetime can be described by MSQI (*Maximal Slicing-Quasi Isotropic*) coordinates [13] which have a line element  $ds^2 = g_{\alpha\beta} dx^\alpha dx^\beta$  of the form:

$$(28) \quad ds^2 = -N^2 dt^2 + A^4 B^{-2} (dr^2 + r^2 d\theta^2) + A^4 B^2 r^2 \sin^2 \theta (d\phi - N^\phi dt)^2.$$

Spacetime is hence fully determined by the four metric potentials  $N$ ,  $N^\phi$ ,  $A$  and  $B$ . MSQI-coordinates are global coordinates and lead to elliptic operators which admit a consistent treatment of boundary conditions and an efficient solution by spectral methods. The matter fields are chosen to model a perfect fluid where first a polytropic, hence analytical, equation of state was used. The assumption of a perfect fluid reduces the equations of motion to an algebraic equation for the heat function  $H$ . From the Einstein equations one derives four elliptic equations for the variables  $\nu = \ln N$ ,  $N^\phi$  and

$$(29) \quad G(r, \theta) = N(r, \theta) A^2(r, \theta) B(r, \theta),$$

$$(30) \quad \zeta(r, \theta) = \nu(r, \theta) + 2\alpha(r, \theta) - \beta(r, \theta)$$

whose final form reads

$$(31) \quad \Delta_3 \nu = \frac{A^4}{B^2} [4\pi(E + S^i_i) + 2(k_1^2 + k_2^2)] - \partial\nu \partial(\nu + 2\alpha + \beta),$$

$$(32) \quad \tilde{\Delta}_3 \tilde{N}^\phi = -16\pi \frac{N}{B^4} \frac{J_\phi}{r \sin \theta} - r \sin \theta \partial N^\phi \partial(6\alpha + 3\beta - \nu),$$

$$(33) \quad \Delta_2 \tilde{G} = 8\pi \frac{N A^6}{B} r \sin \theta (S^r_r + S^\theta_\theta),$$

$$(34) \quad \Delta_2 \zeta = \frac{A^4}{B^2} [8\pi S^\phi_\phi + 3(k_1^2 + k_2^2)] - (\partial\nu)^2$$

where we have introduced  $\alpha = \ln A$ ,  $\beta = \ln B$  and

$$(35) \quad \tilde{G}(r, \theta) = r \sin \theta G(r, \theta),$$

$$(36) \quad \tilde{N}^\phi(r, \theta) = r \sin \theta N^\phi(r, \theta)$$

as well as the abridged notation

$$(37) \quad \partial_\alpha \partial_\beta = \partial_r \alpha \partial_r \beta + \frac{1}{r^2} \partial_\theta \alpha \partial_\theta \beta.$$

Further employed quantities are the total energy density  $E$ , the stress tensor  $S^i_j$ , the momentum density  $J_i$  and  $k_1$ ,  $k_2$  which are related to the extrinsic curvature tensor  $K_{ij}$ .  $\Delta_2$ ,  $\Delta_3$  and  $\tilde{\Delta}_3$  denote scalar Laplacians in two and three dimensions and a vector Laplacian in three dimensions respectively.

Existence and uniqueness of the solution of these elliptic equations are ensured for physically relevant cases [24, 25, 26].

Note that (33) and (34) can be continued analytically to yield genuine 2D-Poisson equations in the entire  $(r, \theta)$ -plane. One infers immediately that  $\zeta$  exhibits a logarithmic divergence for  $r \rightarrow \infty$  unless the total integral over the source of (34) vanishes identically whereas we require  $\zeta|_{r=\infty} = 0$ . This 2D-virial theorem of general relativity (GRV2) [16] is in some sense related to the classical Newtonian virial theorem and furnishes a consistency condition for any solution of the Einstein equations which is compatible with our basic assumptions. It has to be taken into account during the calculation and provides a strong consistency check of the numerical solution.

## 4.2 Numerical method

The mathematical problem involves (31)–(34) and an algebraic first integral equation for the matter fields. Our numerical solutions are exact in the sense that the governing equations are derived from the full theory of general relativity without any analytical approximation while the numerical code solves these equations in all space extending the numerical integration to spatial infinity which allows to impose the exact boundary conditions of asymptotical flatness on the gravitational fields as well as the proper calculation of the source terms of (31)–(34) which fill all space.

This is accomplished by the use of two grids, where the first one covers the stellar interior using the radial variable  $r$  in the interval  $[0, R]$ , while the outer space is compactified thanks to the variable transform  $u = r^{-1}$  and in this way mapping  $[R, \infty]$  onto the finite interval  $[R^{-1}, 0]$ . While in the  $\theta$ -variable a Fourier expansion according to Sec. 2.1 is used, the radial part is expanded in terms of Chebyshev

polynomials. The inner zone is mapped onto half the definition interval  $[0, 1]$  which allows to take into account the parity properties of regular functions with respect to the origin according to Sec. 2.3. In the compactified zone the expansion has been done in the usual manner on the whole definition interval  $[-1, 1]$  of Chebyshev polynomials.

The effective scheme which is based on a relaxation method works as follows. We consider rigidly rotating neutron stars with a polytropic equation of state. A particular configuration is hence determined by fixing the value  $H_c$  of the heat function at the centre of the star and its angular velocity  $\Omega$ . We start from very crude initial conditions where all the metric quantities are set to their flat space values ( $\alpha, \beta, \nu, \zeta$  and  $N^\phi = 0$ ;  $G = 1$ ) and the matter distribution is determined by a first approximate guess.

While the GRV2 identity related to (34) holds for an exact solution of the Einstein equations we have to enforce this consistency relation at each iteration step in order to avoid a logarithmic divergence of the approximate one. This can be accomplished by modifying (34) according to

$$(38) \quad \Delta_2 \zeta = \sigma_\zeta^f + \sigma_\zeta^g \quad \longrightarrow \quad \Delta_2 \zeta = \sigma_\zeta^f + \lambda \sigma_\zeta^g,$$

$$(39) \quad \sigma_\zeta^f = 8\pi \frac{A^4}{B^2} S^\phi_\phi, \quad \sigma_\zeta^g = \frac{A^4}{B^2} [3(k_1^2 + k_2^2)] - (\partial\nu)^2.$$

At each iteration step  $\lambda$  is chosen in such a way that the total source integral vanishes. The final solution has to satisfy (34) exactly which is equivalent to  $\lambda = 1$ . The deviation of  $\lambda$  from unity during the iteration measures the violation of self-consistency of the approximate solution and can be used to monitor convergence.

The sources of (31)–(34) exhibit some terms involving simple operators like  $r$ ,  $\sin \theta$ ,  $\partial_r$ , etc. which are accurately computed in coefficient space before evaluating the entire expressions in configuration space. Expansion of the total sources in terms of the angular eigenfunctions of the different Laplacians ( $P_l^0(\cos \theta)$ ,  $P_l^1(\sin \theta)$  and  $(\cos l\theta, \sin l\theta)$  for  $\Delta_3$ ,  $\tilde{\Delta}_3$ , and  $\Delta_2$  respectively) leads to a system of ODEs in the radial variable. The unique global solution is obtained by appropriate linear combinations of the corresponding particular and homogeneous solutions in order to match the piecewise solutions at the grid interface and to satisfy the boundary conditions at  $r = \infty$ . The new values of the gravitational field variables are then used to update the matter distribution by means of the first integral equation and the iteration can go on.

## 4.3 Tests

We have subjected our code to two different kinds of tests which ensure the reliability of the numerical results.

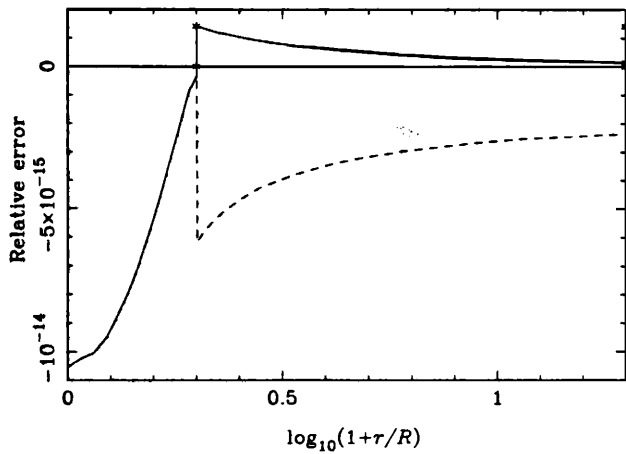


Figure 4: Comparison between numerical and analytical solution for the Schwarzschild interior and exterior incompressible solution. The location of the star surface is indicated by an asterisk. The plotted quantities are the relative error in the pressure with respect to the central pressure inside the star and the absolute error in  $N$  (solid line) and  $A^2$  (dashed line) outside the star.

*External tests* consist in the comparison with previous solutions, either analytical or numerical ones. Such a test of the code has been performed for an analytically known Schwarzschild type solution of a non-rotating homogeneous sphere with the corresponding numerical one. Relative errors committed on global quantities such as total gravitational mass and circumferential radius are of the order of  $10^{-14}$ . This accuracy holds also for local quantities as shown in Fig. 4 for the pressure  $p$  inside the star and the metric coefficients outside the star – none of the errors exceeding  $10^{-14}$ . A recent project of systematic calibration and comparison of the numerical results of different groups working in this field has yielded an agreement of characteristic quantities of realistic neutron star models at a level of about  $10^{-3}$ .

*Internal tests* represent the second important class of tests and are derived from some relations of global or local character which are related to the Einstein equations but not automatically enforced during the calculation. These tests are very powerful, since they do not only verify the proper working of the numerical scheme for some simple – usually degenerate – test problem, but apply to any calculation and supply an intrinsic estimate of the numerical error involved. In the following neutron star matter

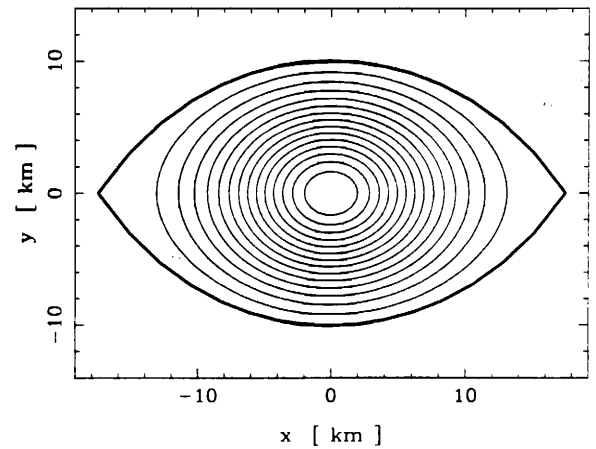


Figure 5: Level contour  $E(r, \theta)$  in the case of a polytropic EOS with  $\gamma=2$  for  $\Omega=\Omega_K$ .

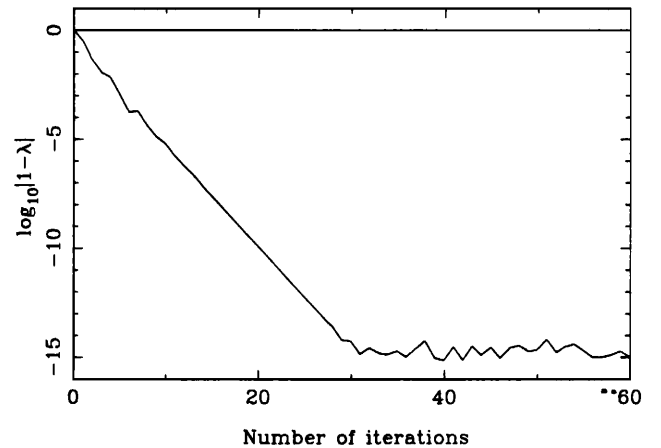


Figure 6: Convergence of the error indicator  $|1-\lambda|$  during the iteration process for  $\Omega=0$ .

was modeled by a perfect fluid with a  $\gamma = 2$  polytropic EOS. The angular velocity has been varied between  $\Omega=0$  for the static case and  $\Omega = \Omega_K$  for the maximum rotating case where for a further increase of  $\Omega$  mass shedding along the equator occurs. Fig. 5 shows the flattened shape of a neutron star rotating at  $\Omega_K$ . A simple test makes use of the known analytical expansion of  $B$  according to  $B = 1 + r^2 \sin^2 \theta f$ . It showed  $B$  to coincide with the analytical value 1 on the polar axis within  $10^{-6}$  in the most

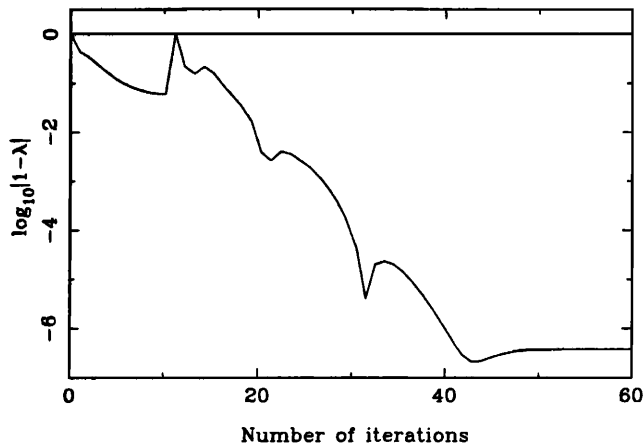


Figure 7: Convergence of the error indicator  $|1-\lambda|$  during the iteration process for  $\Omega = \Omega_K$ . The spike at  $N = 10$  is due to switching on the rotation.

unfavorable case of maximal angular velocity. The principal test is provided by the GRV2 identity. An examination of the Schwarzschild type solution has revealed that  $|1-\lambda|$  is very closely related to the global errors derived from the numerical solution for variable  $N_r$ . This observation, though obtained for the static case, is supposed to hold in the rotating case as well.  $|1-\lambda|$  can thus be considered as an estimator of the global numerical accuracy. Figs. 6, 7 show the convergence of  $|1-\lambda|$  during the iteration for  $\Omega=0$  and  $\Omega=\Omega_K$ . While in the first case the exponential decay of  $|1-\lambda|$  continues until roundoff errors of  $10^{-14}$  mark a lower limit, the total error in the rotating case is about  $10^{-6}$ . This difference is due to the deviation of the flattened stellar shape from the spherical numerical grid which leads to a discontinuity in the derivatives across the stellar surface located *inside* the inner zone, where the diverse quantities hence are no more analytical functions. The attainable accuracy in dependence of the number of grid points is illustrated in Fig. 8. The exponential decrease, usually called *evanescent* error and characteristic for spectral methods, is clearly visible. This property is lost in the rotating case where we observe a power law decay of the committed error  $\propto N_r^{-4.5}$  as found from Fig. 9. This inconvenience will be overcome by the implementation of an adaptive ellipsoidal grid which aligns the domain boundary to the star surface. We finally conclude that we have computed neutron star models with an analytic EOS achieving a precision of  $10^{-14}$  in the static case to some  $10^{-6}$  in the maximum rotation case which has to be compared with

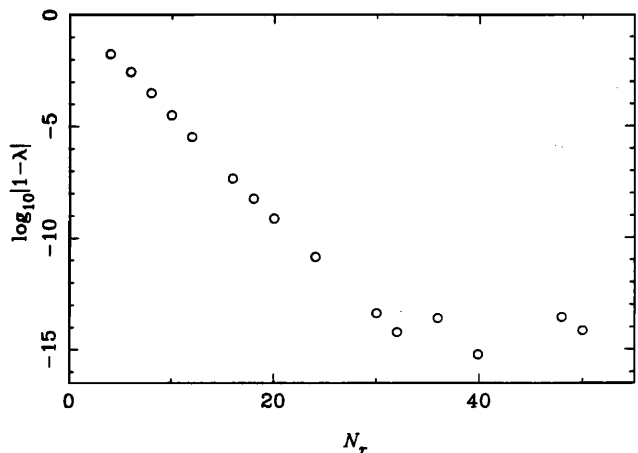


Figure 8: Internal error indicator as a function of  $N_r$  in the compressible spherically symmetric case (polytropic EOS).

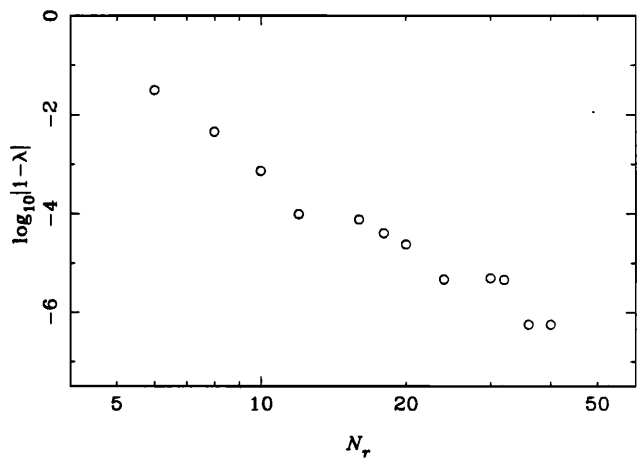


Figure 9: Same as Fig. 8 but for maximal angular velocity  $\Omega_K$ . Pay attention to the log – log scale; the spectral properties are lost here and one observes a power law convergence.

previous results based on finite difference methods of the order of  $10^{-2}$  [27, 28, 29, 30].

It is further interesting to note that for typical values of  $N_r = 32$  and  $N_\theta = 16$  one iteration is performed in 480 ms on a VAX 4500. For an average number of 50 iterations per model the whole calculation is finished in about 24 s. The code efficiency has enabled us to carry out extensive studies

of neutron star samples under employment of numerous realistic EOS of neutron star matter [14].

#### 4.4 Rotating neutron stars with magnetic field

A further step toward a realistic description of rapidly rotating neutron stars has been recently achieved by the fully self-consistent inclusion of magnetic fields into our models [15]. These calculations represent the first numerical solutions of the coupled 2D–Einstein–Maxwell equations for rotating neutron stars which are hence fully relativistic, taking into account any kind of interaction of the electromagnetic field with the star and the gravitational field.

To complete the physical specification of our neutron star models as described in Sec. 4.2 we assume a perfect conductor behavior of neutron star matter – the star interior is thus free of electric fields – and add the electromagnetic field variables  $A_t$ ,  $A_\phi$ , the current variables  $j_t$  and  $j_\phi$  and a structure function  $f$  which determines the current distribution inside the star. The additional free parameter which fixes a unique neutron star configuration is the total electric charge  $Q$ . A derived global quantity is the magnetic dipole moment  $\mathcal{M}$  which characterizes the magnetic properties of the neutron star. The Maxwell equations lead to a set of coupled elliptic partial differential equations which exhibits a similar structure as (31)–(34). They involve a scalar Poisson equation for  $A_t$  and a vector Poisson equation for  $A_\phi$  which read

$$(40) \quad \Delta_3 A_t = -\mu_0 \frac{A^4}{B^2} (g_{tt} j^t + g_{t\phi} j^\phi) - \frac{A^4 B^2}{N^2} N^\phi r^2 \sin^2 \theta \times \partial A_t \partial N^\phi - \left( 1 + \frac{A^4 B^2}{N^2} (r \sin \theta N^\phi)^2 \right) \times \partial A_\phi \partial N^\phi - (\partial A_t + 2N^\phi \partial A_\phi) \partial(2\alpha + \beta - \nu) - 2 \frac{N^\phi}{r} \left( \partial_r A_\phi + \frac{1}{r \tan \theta} \partial_\theta A_\phi \right),$$

$$(41) \quad \tilde{\Delta}_3 \tilde{A}^\phi = -\mu_0 A^8 (j^\phi - N^\phi j^t) r \sin \theta + \frac{A^4 B^2}{N^2} r \sin \theta \partial N^\phi (\partial A_t + N^\phi \partial A_\phi) + \frac{1}{r \sin \theta} \partial A_\phi \partial(2\alpha + \beta - \nu)$$

where we define

$$(42) \quad \tilde{A}^\phi = \frac{A_\phi}{r \sin \theta}.$$

In this extended formulation the determination of  $A_t$  and

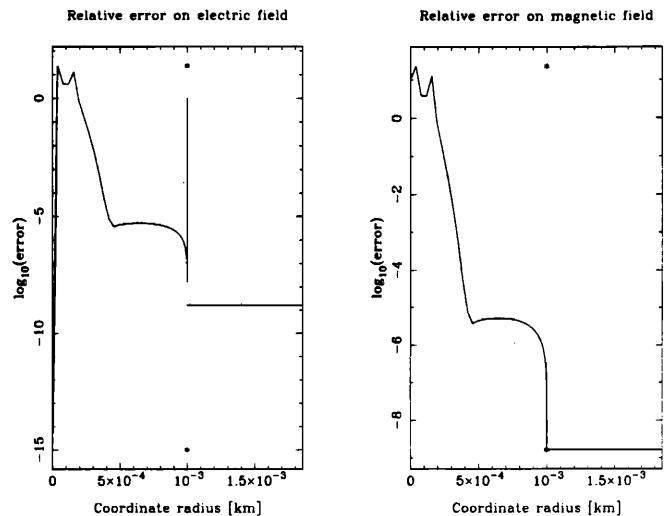


Figure 10: Comparison between the exact and the numerical solution in the case of a rotating conducting sphere with a magnetic point dipole at its centre. The asterisks indicate the sphere’s surface.

$A_\phi$  precedes the solution of the former set of equations.  $A_\phi$  is a smooth function in all space – we recall that  $\mu_r \simeq 1$  for neutron star matter – and can therefore be uniquely solved by imposing the asymptotic boundary condition  $A_\phi \rightarrow 0$  for  $r \rightarrow \infty$ . The treatment of  $A_t$  is slightly more complicated due to its non-smoothness across the stellar surface – a behavior caused by the surface charges which are characteristic for ideal conductors. Since  $A_t$  is linked to  $A_\phi$  by a linear relation in the star interior, the exterior solution has to be matched to the latter one, respecting the condition  $A_t = 0$  at infinity. We note that, once more, this is a task which is easily performed thanks to the use of a spectral method. After solution of the whole system we can update the electromagnetic contributions to the stress–energy tensor and proceed with the solution of the Einstein equations according to Sec. 4.2.

Test calculations of the electromagnetic part have been performed for some simple cases, where analytical solutions are known, among these one involving a rotating magnetic dipole where an infinitesimal current loop at the origin is surrounded by some rotating perfectly conducting sphere. This testbed calculation mimics the configuration of a rotating neutron star with surface charges. Fig. 10 shows the relative error committed on the electric and the magnetic field for a conducting sphere of 1 m radius rotating at  $\Omega = 3000 \text{ s}^{-1}$  with a central current loop of  $j_0 = 10^{11} \text{ Am}^{-2}$ . Apart from the origin where the model current differs from the theoretical  $\delta$ -distribution the relative error is

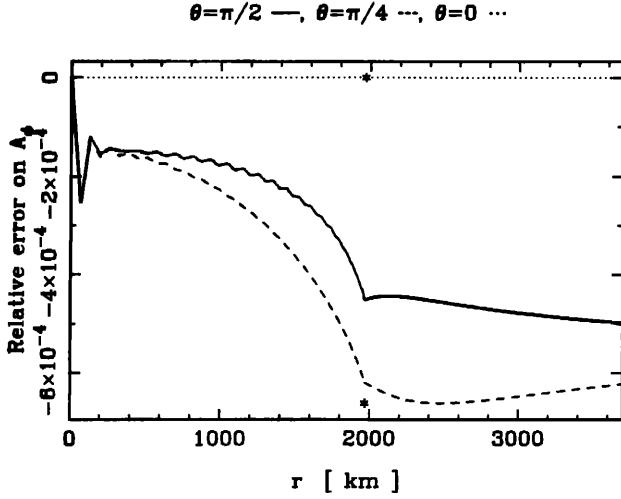


Figure 11: Comparison between Ferraro’s analytical solution and the numerical one in the case of a Newtonian incompressible fluid endowed with a magnetic field corresponding to a constant current function  $f(x) = f_0$ . The plotted quantity is the relative difference between the two values of  $A_\phi$  as a function of the radial coordinate  $r$  for three values of  $\theta$ . Asterisks indicate the star surface.

very small: about  $10^{-5}$  at half the radius and reaching its minimal value of  $10^{-9}$  outside the sphere. An analytical solution for a Newtonian incompressible fluid [31] endowed with a particular current distribution under the – simplifying – assumption of spherical symmetry was adopted as a more sophisticated test. Also in this case the agreement was quite good with a relative error of better than  $10^{-3}$ , shown in Fig. 11. The deterioration with respect to the dipole problem is due to some simplifying assumptions of the analytical model.

The accuracy of solutions of the complete Einstein–Maxwell equations was estimated as in Sec. 4.2 by use of the virial identity GRV2 [17] as well as by a more general three dimensional integral identity valid for any stationary and asymptotically flat spacetime which we call GRV3 [18]. It is the general relativistic generalization of the classical Newtonian virial theorem. The actual values of  $|1-\lambda|$  showed about  $10^{-5}$  for analytical EOS and some  $10^{-4}$  for the tabulated ones which agree with those of calculations without magnetic field. Throughout all the calculations we chose a grid resolution of 41 points in  $r$  and 21 points in  $\theta$ .

In the following we studied configurations of *static* neutron stars endowed with a magnetic field. The absence of kinematical effects allows an unambiguous interpretation

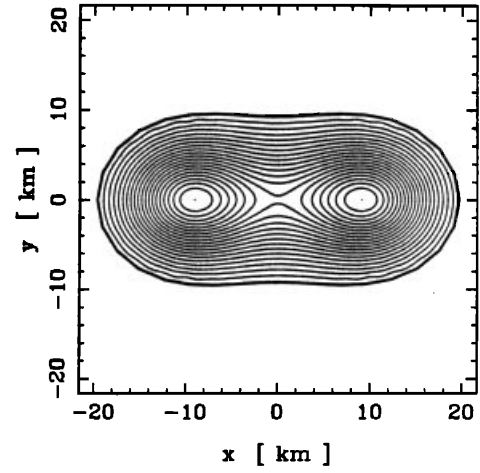


Figure 12: Fluid proper density isocontours in the  $(r, \theta)$ –plane for the  $M = 4.06M_\odot$  maximum mass static magnetized star built upon a polytropic EOS for  $\gamma = 2$ . The thick line indicates the star surface.

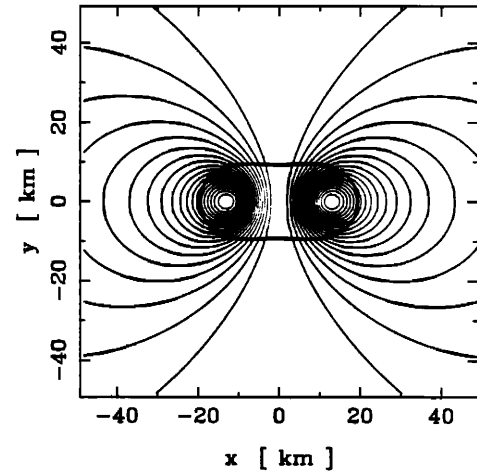


Figure 13: Magnetic field lines in the  $(r, \theta)$ –plane for the maximum mass configuration corresponding to Fig. 12. The thick line indicates the star surface. The magnetic field amplitude amounts to  $B_C = 9 \times 10^4$  GT at the star’s centre.

of the effects of the magnetic field. In the static case the electric charge vanishes identically, leaving alone a magnetic field. Since the stress–energy tensor is *not* isotropic, we observe a deformation of the star already in the static case. Fig. 12 shows a maximum field configuration and

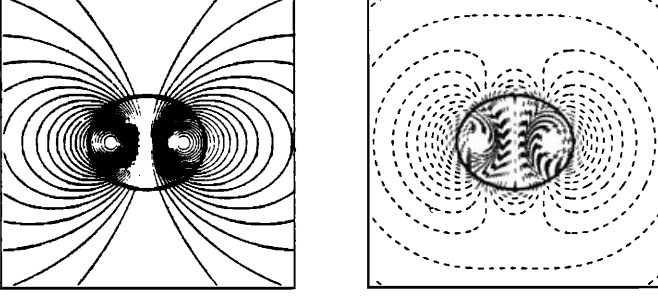


Figure 14: a. Magnetic field lines in the  $(r, \theta)$ -plane for the configuration specified in the text. The thick line indicates the star surface. b. Electric isopotential lines  $A_t = \text{const}$ .

Fig. 13 the corresponding distribution of the magnetic field. In the *rotating* case the magnetic field is accompanied by an additional electric field. The both field distributions for a Pol2  $M = 3.37M_\odot$  model at  $\Omega = 3 \times 10^3 \text{ rad s}^{-1}$  and a constant current function are given in Fig. 14. Note that the field lines of  $A_t$  and  $A_\phi$  coincide in the star interior due to the perfect conductor assumption. The non-smoothness of  $A_t$  across the star boundary properly reflects the discontinuity of the electric field due to the existing surface charges.

## 5 3D-gravitational neutron star collapse

### 5.1 Basic equations

The investigation of the 3D-gravitational collapse of rotating neutron stars requires the solution of the general time-dependent field equations of general relativity. We stress that already in the Newtonian case a fully three dimensional simulation of stellar collapse is a highly demanding and non-trivial problem. Indeed up to this day there exists only one corresponding investigation which aimed at the study of gravitational wave emission associated with type II supernovae [32]. While in the presence of symmetries like stationarity or axisymmetry the field equations are greatly simplified when evaluated explicitly for some appropriate coordinates the situation is quite contrary for a three dimensional dynamical problem. It is therefore favorable to solve the Einstein equations in their original coordinate independent (covariant) form. This choice allows us to adopt elliptic equations for the gauge variables  $N$  and  $N^i$  which have a direct geometrical signification. The *maximal slicing-minimal distortion gauge* [24, 7] is

highly singularity avoiding and neatly captures the propagation of gravitational waves in the far field zone. This is a very important feature, since the study of gravitational wave emission is the principal goal of this investigation.

The governing equations then have the following form:

$$(43) \quad \partial_t h_{ij} + N_{i|j} + N_{j|i} + 2NK_{ij} = 0,$$

$$(44) \quad \partial_t K^i_j + N^l K^i_{j,l} - N^i_{,l} K^l_j + N^l_{,j} K^i_l + N^i_{|j} - N[R^i_j + 4\pi(S - E)\delta^i_j - 8\pi S^i_j] = 0,$$

$$(45) \quad R - K^i_j K^j_i - 16\pi E = 0,$$

$$(46) \quad K^j_{i|j} - 8\pi J_i = 0,$$

$$(47) \quad \partial_t E + N^l E_{,l} - NK^i_j S^j_i + N^{-1}(N^2 J^i)_{|i} = 0,$$

$$(48) \quad \partial_t J_i + N^l J_{i,l} + N^l_{,i} J_l + (E\delta^j_i + S^j_i)N_{|j} + NS^j_{i|j} = 0,$$

$$(49) \quad N^l_{|l} - N[K^i_j K^j_i + 4\pi(E + S)] = 0,$$

$$(50) \quad N^{i|j}_{|j} + \frac{1}{3}(N^j_{|j})^i + R^i_j N^j + 2K^{ij}N_{|j} + 16\pi N J^i = 0.$$

This system of coupled partial differential equations is characterized by the following properties:

The system includes a time first order hyperbolic system (43) and (44) of the spatial metric tensor  $h_{ij}$  and its conjugate momentum variable  $K_{ij}$  which reduces to a wave equation for  $h_{ij}$  in the far field zone. The evolution of the matter fields  $E$  and  $J_i$  is governed by the parabolic system (47) and (48). These equations constitute the dynamical part of our problem.  $N$  and  $N^i$  are subjected to the Poisson type equations (49) and (50) where the matter fields act as source terms. Further involved quantities are the stress tensor  $S_{ij}$  and the Ricci tensor  $R_{ij}$  where  $S = S^i_i$  and  $R = R^i_i$ . The additional constraint equations (45) and (46) which establish some consistency relations between gravitational and matter fields are satisfied identically for the exact solution. They may be used to reduce the number of the dynamical variables, an approach that would result in a *constrained* evolution scheme. Indeed this procedure guarantees that the numerical solution represents at any moment some solution of the Einstein equations but not necessarily the correct one. We prefer an unconstrained scheme where the constraint equations can serve to estimate the involved numerical errors.

### 5.2 Numerical method

In the spirit of the analytical approach of Sec. 5.1 we have opted for a numerical scheme which is based on a one-to-one adaptation of common tensor calculus, where elementary operations like contraction and covariant derivation

are performed by specific subroutines acting on entire tensor quantities. We further introduce a flat background metric which enables us to separate the contributions related to the curvature of space and to carry out the numerical operations with respect to flat space spherical coordinates and the corresponding metric tensor  $f_{ij}$  [33]. For a given three-metric  $h_{ij}$  we then have the following relations:

We first introduce a tensor  $\Delta^i{}_{jk}$  defined as

$$(51) \quad \Delta^i{}_{jk} = \frac{1}{2} h^{il} (h_{jl||k} + h_{kl||j} - h_{jk||l})$$

where  $\parallel$  denotes covariant differentiation with respect to flat space spherical coordinates. The covariant derivative  $U^i{}_{||j}$  of a vector  $U^i$  in curved three-space can then be re-expressed as

$$(52) \quad U^i{}_{||j} = U^i{}_{||j} + \Delta^i{}_{jk} U^k$$

where the generalization to tensors of higher order is obvious. We can further rewrite the Ricci tensor  $R_{ij}$  in terms of the  $\Delta^i{}_{jk}$ .

$$(53) \quad R_{ij} = \Delta^l{}_{ij||l} - \Delta^l{}_{j||i} + \Delta^l{}_{ij} \Delta^m{}_{lm} - \Delta^l{}_{im} \Delta^m{}_{jl}.$$

The effective use of our scheme is clarified by inspection of the already familiar scalar Poisson equation.

$$(54) \quad N^{|i}{}_{|i} = S \iff h^{ij} (N_{||ij} - \Delta^m{}_{ij} N_{||m}) = S.$$

Defining a new tensor field  $\mathbf{r}$  as  $h^{ij} = f^{ij} + r^{ij}$  we can isolate the  $(f_{ij})$ -related covariant Laplacian and find the biometric equivalent of the covariant scalar Poisson equation

$$(55) \quad N^{|i}{}_{|i} = S + (f^{ij} + r^{ij}) \Delta^m{}_{ij} N_{||m} - r^{ij} N_{||ij}.$$

In the case of a conformally flat metric  $h_{ij} = A^4 f_{ij}$  with  $f_{ij}$  being the usual metric tensor of flat space spherical coordinates we obtain  $r^{ij} = (A^{-4} - 1) f^{ij}$  and the following equation where  $\Delta_f$  represents the usual flat space scalar Laplacian ( $\alpha$  denotes  $\ln A$ ).

$$(56) \quad \Delta_f N = S - 2A^{-4} (\partial_r \alpha \partial_r N + \frac{1}{r^2} \partial_\theta \alpha \partial_\theta N + \frac{1}{r^2 \sin^2 \theta} \partial_\phi \alpha \partial_\phi N) - (A^{-4} - 1) \Delta_f N.$$

The linear contributions on the right can be eliminated, if we slightly change the definition of  $\mathbf{r}$  to describe the deviation of the conformal metric  $\tilde{h} = \gamma^{-1} h$  from the flat space metric  $f$ , where  $\gamma^3 = |h| |f|^{-1}$ . So with  $\tilde{h}^{ij} = f^{ij} + r^{ij}$  we have  $\mathbf{r} = 0$  and

$$(57) \quad \Delta_f N = A^4 S - 2 (\partial_r \alpha \partial_r N + \frac{1}{r^2} \partial_\theta \alpha \partial_\theta N + \frac{1}{r^2 \sin^2 \theta} \partial_\phi \alpha \partial_\phi N).$$

Though this result has been derived for a conformally flat metric we conclude that for any three-space the separation of the conformal factor is a first improvement compared to the flat space approximation.

Following our reasoning in Sec. 2.1 we restrict ourselves to the exclusive use of *pseudophysical* components of tensor quantities related to the standard local orthonormal frame of flat space spherical coordinates in our numerical scheme. The subroutines which calculate the covariant derivatives of tensors of order zero to three appearing in our equations show the typical relative errors of the order of  $10^{-14}$  due to roundoff errors when using simple test functions. For a successive derivation of a scalar function down to a tensor of order four the relative error still does not exceed  $10^{-12}$ . While the computation of the lapse equation can be reduced to the iterative solution of a scalar Poisson-like equation as demonstrated in Sec. 4.2, there remain two other problems of higher demand. The first one concerns the solution of the general shift vector equation involving a linear vector operator which comprises a vector Laplacian and the gradient of a divergence applied to the shift vector  $N^i$ . In Sec. 5.3 we present a decomposition scheme based on the Clebsch-Gordan theorem which leads to an equivalent system of three scalar Poisson equations that can be solved successively. The other one is related to the semi-implicit time integration of the evolution equations of the metric potentials. Here  $R_{ij}$  includes a tensor Laplacian  $\Delta h_{ij}$  which has to be treated implicitly. An equivalent approach as in the vector case is in work.

### 5.3 Vector Poisson equation

The numerical inversion of a 3D-vector Poisson equation is necessary to solve the general shift vector equation which is an equation of the following type

$$(58) \quad \Delta \mathbf{V} + \alpha \nabla (\nabla \cdot \mathbf{V}) = \mathbf{S}$$

where  $\alpha$  is a constant. In order to facilitate the solution of (58) we decompose  $\mathbf{V}$  and  $\mathbf{S}$  into its divergence-free and its irrotational part. We introduce vector fields  $\tilde{\mathbf{V}}$  and  $\tilde{\mathbf{S}}$  which we suppose to be divergence-free as well as two scalar potentials  $\Psi$  and  $\Phi$ . We thus have a *unique* decomposition

$$(59) \quad \mathbf{V} = \tilde{\mathbf{V}} + \nabla \Psi$$

$$(60) \quad \mathbf{S} = \tilde{\mathbf{S}} + \nabla \Phi$$

after specifying the appropriate boundary conditions for  $\Phi$  and  $\Psi$ . In a first step we solve the Poisson equation for  $\Phi$  which we obtain by taking the divergence of (60).

$$(61) \quad \Delta \Phi = \nabla \cdot \mathbf{S}.$$

Rewriting (58) in terms of the new variables we infer the equivalent equation

$$(62) \quad \Delta \tilde{V} + \nabla((1+\alpha)\Delta\Psi - \Phi) = \tilde{S}.$$

Taking the divergence of (62) where we make use of the commutativity of differential operators in flat space, we find a Poisson equation linking  $\Delta\Psi$  to the already known potential  $\Phi$ .

$$(63) \quad (1+\alpha)\Delta\Delta\Psi = \Delta\Phi.$$

The solution of (63) is a priori determined up to an additional potential  $\Phi_H$  with  $\Delta\Phi_H = 0$ . We fix  $\Phi_H$  to be zero according to the boundary conditions and obtain a Poisson equation for  $\Psi$ .

$$(64) \quad (1+\alpha)\Delta\Psi = \Phi.$$

We turn now to (62). Taking into account (64) we derive the final equation that governs the divergence-free fraction of  $V$ .

$$(65) \quad \Delta \tilde{V} = \tilde{S}.$$

We specify the components  $V_i$  to be the physical components of the vector  $V$  related to the local orthonormal basis of spherical coordinates. We further drop the tildes on the vector quantities. The explicit write-up of (65) then reads

$$(66) \quad \Delta_f V_r - \frac{2}{r^2} V_r - \frac{2}{r^2} \left( \partial_\theta + \frac{1}{\tan\theta} \right) V_\theta - \frac{2}{r^2 \sin\theta} \partial_\phi V_\phi = S_r,$$

$$(67) \quad \Delta_f V_\theta - \frac{1}{r^2 \sin^2\theta} V_\theta + \frac{2}{r^2} \partial_\theta V_r - \frac{2}{r^2 \sin\theta \tan\theta} \partial_\phi V_\phi = S_\theta,$$

$$(68) \quad \Delta_f V_\phi - \frac{1}{r^2 \sin^2\theta} V_\phi + \frac{2}{r^2 \sin\theta} \partial_\phi V_r + \frac{2}{r^2 \sin\theta \tan\theta} \partial_\phi V_\theta = S_\phi$$

where  $\Delta_f$  denotes the ordinary scalar Laplacian

$$(69) \quad \Delta_f = \partial_r^2 + \frac{2}{r} \partial_r + \frac{1}{r^2 \tan\theta} \partial_\theta + \frac{1}{r^2} \partial_\theta^2 + \frac{1}{r^2 \sin^2\theta} \partial_\phi^2.$$

We further recall the representation of the covariant divergence  $\nabla \cdot S$  in spherical coordinates

$$(70) \quad \nabla \cdot S = \partial_r S_r + \frac{2}{r} S_r + \frac{1}{r} \partial_\theta S_\theta + \frac{1}{r \tan\theta} S_\theta + \frac{1}{r \sin\theta} \partial_\phi S_\phi.$$

We adopt the following notation where we introduce two auxiliary scalar potentials  $U$  and  $W$  in order to obtain a set of decoupled equations which is equivalent to (66)–(68).

$$(71) \quad V_\theta = \frac{1}{r} \partial_\theta U - \frac{1}{r \sin\theta} \partial_\phi W,$$

$$(72) \quad V_\phi = \frac{1}{r} \partial_\theta W + \frac{1}{r \sin\theta} \partial_\phi U.$$

From  $\nabla \cdot V = 0$  we get

$$(73) \quad \partial_r V_r + \frac{2}{r} V_r + \frac{1}{r^2} \partial_\theta^2 U + \frac{1}{r^2 \tan\theta} \partial_\theta U + \frac{1}{r^2 \sin^2\theta} \partial_\phi^2 U = 0.$$

Combining (73) with (66) leads us to a scalar Poisson equation for  $\tilde{V}$  where we have defined  $\tilde{V} = rV_r$ .

$$(74) \quad \Delta_f \tilde{V} = rS_r.$$

Proceeding in the same manner with (67) and (68) we derive the following linear combinations of the resulting equations with (73).

$$(75) \quad \sin\theta \partial_\theta (\partial_r^2 U - \partial_r V_r) - \partial_\phi \left( \Delta W - \frac{2}{r} \partial_r W \right) = r \sin\theta S_\theta,$$

$$(76) \quad \frac{1}{\sin\theta} \partial_\phi (\partial_r^2 U - \partial_r V_r) + \partial_\theta \left( \Delta W - \frac{2}{r} \partial_r W \right) = r S_\phi.$$

Derivation of (75) with respect to  $\theta$  and of (76) with respect to  $\phi$  and adding the both equations allows us to recover a scalar Poisson equation for  $(\partial_r U - V_r)$  which only involves the angular variables  $(\theta, \phi)$  where we have integrated over  $r$  and set the implied integration constant to zero to assure a vanishing behavior of the source terms at  $r = \infty$ .

$$(77) \quad \Delta_{\theta\phi} (\partial_r U - V_r) = -r^2 S_r.$$

Here  $\Delta_{\theta\phi}$  denotes the angular fraction of  $\Delta_f$  multiplied by  $r^2$ .

At this point we can determine  $U$  by means of  $V_r$  which has already been fixed by (74). In order to calculate the lacking potential  $W$  we take up (76). An ordinary integration over  $\theta$  where we require vanishing behavior of the source terms at infinity as for  $(\partial_r U - V_r)$  results in a scalar Poisson equation for  $\tilde{W}$  defined by  $W = r\tilde{W}$ ,

$$(78) \quad r\Delta\tilde{W} = \int_0^\theta \left[ rS_\phi - \frac{1}{\sin\theta} \partial_\phi (\partial_r^2 U - \partial_r V_r) \right] d\theta.$$

This scheme hence allows to compute the required potentials successively for a given source distribution starting

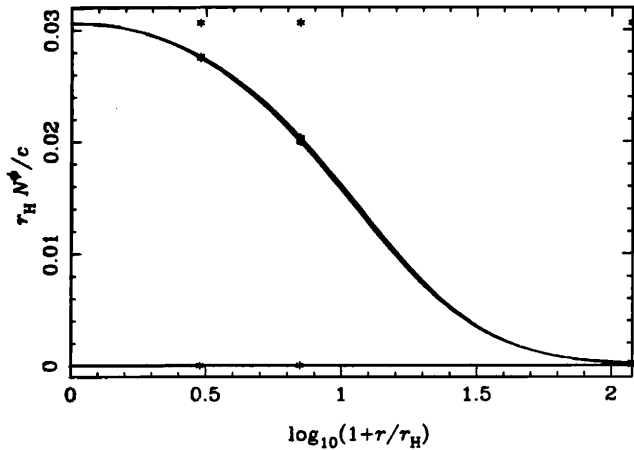


Figure 15:  $N^\phi$  for a rapidly rotating Kerr black hole at  $a/M = 0.99$  where  $r_H$  denotes the radius of the horizon. The different curves correspond to various values of  $\theta$  ranging from  $0^\circ$  to  $90^\circ$ . The asterisks indicate the subdomain boundaries.

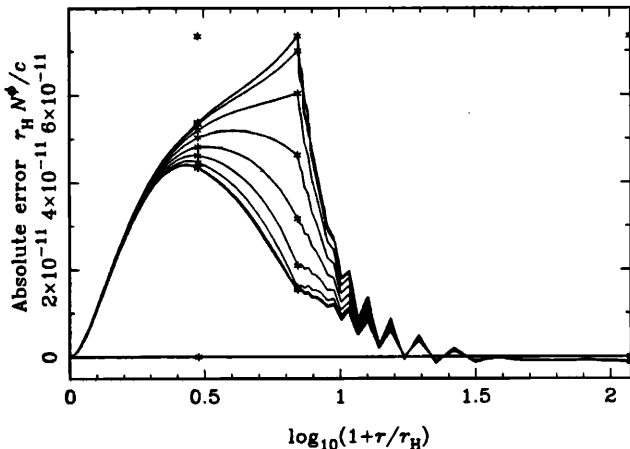


Figure 16: Absolute error in  $N^\phi$  corresponding to Fig. 15.

from the ordinary Poisson equation for  $\tilde{V}$ , solving then the equation involving  $(\partial_r U - V_r)$  and thus fixing  $U$  while in a last step  $\tilde{W}$  can be determined as a quantity depending on  $V_r$  and  $U$ . Note that  $S_\theta$  does not appear in the source terms of the final equations. This is due to the constraint equation  $\nabla \cdot \mathbf{S} = 0$  removing one degree of freedom.

## 5.4 Tests

The routines we have built based on this computation scheme and on our spectral method library enable us to solve a vector Poisson equation in a multidomain configuration including an exterior compactified zone – if desired – which covers all space and thus allows to impose proper boundary conditions for asymptotically flat space where for the time being we restrict ourselves to the supersymmetric case. Numerical tests have been performed on simple test functions and on problems where the analytical solution was known in advance. For test functions we found once more the numerical error to be governed by the roundoff limit of the employed machine of the order of  $10^{-14}$ . As an advanced test problem we solved the shift vector equation in the Kerr metric of a rotating black hole. The presented configuration corresponds to a rapidly rotating Kerr hole –  $a/M \simeq 0.99$  – close to maximum angular velocity where the relativistic effects involving the shift vector component  $N^\phi$  are strongly pronounced. The entire space outside the black hole is covered by three zones where the outer compactified one extends to spatial infinity. The grid resolution is chosen to be  $N_r = 33$  in each zone and  $N_\theta = 9$ . Note the quite small number of nodes in  $\theta$ . Thanks to taking into account the even symmetry of the problem with respect to reflection at the equatorial plane according to Sec. 2.2 this corresponds to an effective value of 17 in the whole interval  $[0, \pi]$ . Fig. 15 shows the course of  $N^\phi$  in the vicinity of the black hole while Fig. 16 illustrates the absolute error committed on the shift vector component  $N^\phi$ . The numerical error nowhere exceeds  $10^{-10}$ . For a higher value of  $N_r$  it even goes down to about  $10^{-13}$ . As expected the numerical errors are most elevated at the boundaries of the different subdomains where the piecewise solutions of adjacent shells are matched. The GRV2 identity which had already proved its usefulness in the study of axisymmetric stationary neutron stars was applied to estimate the total error of the numerically computed Kerr spacetime. The error estimator  $|1 - \lambda|$  turned out to be closely related to the numerical errors derived above from comparison with the analytical solution and confirmed in this highly relativistic problem to be a sensitive indicator of the global numerical accuracy.

## 6 Conclusion

We have presented the application of spectral methods to several problems of numerical relativity. In each case they proved to be a highly valuable tool which lead to results typically several orders of magnitude more accurate than corresponding codes based on finite difference

schemes. Especially in spherical-like coordinates the advantages of a spectral method which allows a rigorous treatment of the associated regularity conditions, while improving the efficiency of the code at the same time, are remarkable. Particularly important properties for our problems are the negligible numerical viscosity in temporal evolution schemes which enabled us to capture subtle details in the time-dependence of evolved variables as observed for equilibrium configurations of neutron stars in Sec. 3.3, as well as the very natural treatment of boundary conditions and the efficient solution of elliptic equations which is a frequently encountered task in our investigations. Our so far very positive experiences with spectral methods give us confidence to dispose of the appropriate numerical tool to tackle the exciting problem of black hole formation by 3D-gravitational collapse of neutron stars.

## 7 Acknowledgments

J. Frieben gratefully acknowledges financial support by the GOTTLIEB DAIMLER – UND KARL BENZ – STIFTUNG.

## References

- [1] L.L. Smarr ed., *Sources of Gravitational Radiation*, Cambridge University Press, Cambridge, 1979.
- [2] C.R. Evans, L.S. Finn, D.W. Hobill eds., *Frontiers in numerical relativity*, Cambridge University Press, Cambridge, 1989.
- [3] R. d’Inverno ed., *Approaches to Numerical Relativity*, Cambridge University Press, Cambridge, 1992.
- [4] A. Abramovici et al., *LIGO: the laser interferometer gravitational-wave observatory*, *Science*, 256 (1992), pp. 325–333.
- [5] C. Bradaschia et al., *The VIRGO project: a wide band antenna for gravitational wave detection*, *Nucl. Instr. and Meth. A*, 289 (1990), pp. 518–525.
- [6] J. Hough, K. Danzmann, *Proposal for a 600 m Laser-Interferometric Gravitational Wave Antenna*, unpublished, 1994.
- [7] L. Smarr, J.W. York, *Kinematical conditions in the construction of spacetime*, *Phys. Rev. D*, 17 (1978), pp. 2529–2551.
- [8] S. Bonazzola, J.A. Marck, *Pseudo-spectral technique applied to numerical solutions for stellar collapse*, *Astron. Astrophys.*, 164 (1986), pp. 300–309.
- [9] S. Bonazzola, J.A. Marck, *Three-dimensional gas dynamics in a sphere*, *J. Comp. Phys.*, 87 (1990), pp. 201–230.
- [10] E. Gourgoulhon, *Simple equations for general relativistic hydrodynamics in spherical symmetry applied to neutron star collapse*, *Astron. Astrophys.*, 252 (1991), pp. 651–663.
- [11] E. Gourgoulhon, P. Haensel, *Upper bounds on the neutrino burst from collapse of a neutron star into a black hole*, *Astron. Astrophys.*, 271 (1993), pp. 187–208.
- [12] E. Gourgoulhon, P. Haensel, D. Gondek, *Maximum mass instability of neutron stars and weak interaction processes in dense matter*, *Astron. Astrophys.*, 294 (1995), pp. 747–756.
- [13] S. Bonazzola, E. Gourgoulhon, M. Salgado, J.A. Marck, *Axisymmetric rotating relativistic bodies: a new numerical approach for “exact” solutions*, *Astron. Astrophys.*, 278 (1993), pp. 421–443.
- [14] M. Salgado, S. Bonazzola, E. Gourgoulhon, P. Haensel, *High precision rotating neutron star models*, *Astron. Astrophys.*, 291 (1994), pp. 155–170.
- [15] M. Bocquet, S. Bonazzola, E. Gourgoulhon, J. Novak, *Rotating neutron star models with a magnetic field*, *Astron. Astrophys.*, 301 (1995), pp. 757–775.
- [16] S. Bonazzola, *The virial theorem in general relativity*, *Astrophys. J.*, 182 (1973), pp. 335–340.
- [17] S. Bonazzola, E. Gourgoulhon, *A virial identity applied to relativistic stellar models*, *Class. Quantum Grav.*, 11 (1994), pp. 1775–1784.
- [18] E. Gourgoulhon, S. Bonazzola, *A formulation of the virial theorem in general relativity*, *Class. Quantum Grav.*, 11 (1994), pp. 443–452.
- [19] J.A. Marck, A. Lioure, S. Bonazzola, *Numerical study of the tidal interaction of a star and a massive black hole*, *Astron. Astrophys.*, 306 (1996), pp. 666–674.
- [20] J.M. Bardeen, T. Piran, *General relativistic axisymmetric rotating systems: coordinates and equations*, *Phys. Rep.*, 96 (1983), pp. 205–250.
- [21] S. Lanczos, *Applied Analysis*, Prentice-Hall, Englewood Cliffs, N. J., 1956.
- [22] J.R. Oppenheimer, H. Snyder, *On continued gravitational contraction*, *Phys. Rev.*, 56 (1939), pp. 455–459.

- [23] P.J. Schinder, *General relativistic implicit radiation hydrodynamics in polar sliced space-time*, in *Frontiers in numerical relativity*, Cambridge University Press, Cambridge, 1989, pp. 163–170.
- [24] L. Smarr, J.W. York, *Radiation gauge in general relativity*, *Phys. Rev. D*, 17 (1978), pp. 1945–1956.
- [25] M. Cantor, *Some problems of global analysis on asymptotically simple manifolds*, *Compos. Math.*, 38 (1979), pp. 3–35.
- [26] M. Cantor, *The existence of non-trivial asymptotically flat initial data for vacuum spacetimes*, *Commun. Math. Phys.*, 57 (1977), pp. 83–96.
- [27] J.L. Friedman, J.R. Ipser, L. Parker, *Rapidly rotating neutron star models*, *Astrophys. J.*, 304 (1986), pp. 115–139.
- [28] H. Komatsu, Y. Eriguchi, I. Hachisu, *Rapidly rotating general relativistic stars – I. Numerical method and its application to uniformly rotating polytropes*, *MNRAS*, 237 (1989), pp. 355–379.
- [29] H. Komatsu, Y. Eriguchi, I. Hachisu, *Rapidly rotating general relativistic stars – II. Differentially rotating polytropes*, *MNRAS*, 239 (1989), pp. 153–171.
- [30] G.B. Cook, S.L. Shapiro, S.A. Teukolsky, *Spin-up of a rapidly rotating star by angular momentum loss: effects of general relativity*, *Astrophys. J.*, 398 (1992), pp. 203–223.
- [31] V.C.A. Ferraro, *On the equilibrium of magnetic stars*, *Astrophys. J.*, 119 (1954), pp. 407–412.
- [32] S. Bonazzola, J.A. Marck, *Efficiency of gravitational radiation from axisymmetric and 3D stellar collapse*, *Astron. Astrophys.*, 267 (1993), pp. 623–633.
- [33] N. Rosen, *Flat-space metric in general relativity theory*, *Ann. Phys.*, 22 (1963), pp. 1–11.

